Supplementary Materials for Wetting Transition of Water on Monolayer Coated Materials

Keywords: Wetting Transition, Wetting Transparency, Monolayer Coatings, 2D Materials, Wetting, Translucency, Phase Transition

S1 Modeling Complex Dispersions of substrates

Complex dielectric functions $\varepsilon(i\omega)$ are obtained from optical constants n and k, via the Kramers-Kronig relation,

$$\varepsilon_j(i\omega) = 1 + \frac{2}{\pi}\int_0^\infty \frac{x\varepsilon_{2j}(x)}{x^2+\omega^2}dx \tag{S1}$$

where $\varepsilon_{2\perp,\parallel} = 2n_{\perp,\parallel}k_{\perp,\parallel}$ and $j = \parallel, \perp$ for anisotropic substrates. We use the geometric mean $\bar{\varepsilon}(i\omega) = [\varepsilon_\parallel(i\omega)\cdot\varepsilon_\perp(i\omega)]^{1/2}$ for all our substrates[1]. The permittivity $\varepsilon(i\omega)$ is fitted using the insulator model[2]

$$\varepsilon(i\omega) = 1 + (\eta^2 - 1)/(1 + \omega^2/\omega_e^2) \tag{S2}$$

where η and ω_e are fitting parameters representing the refractive index at optical frequencies and a characteristic electron absorption frequency, for 4H−SiC, diamond, sapphire, quartz, and glass. We use an empirical ten-oscillator fit for the $\varepsilon(i\omega)$ of water,

HOPG, and the TMDs:

$$\varepsilon(i\omega) = 1 + \sum_{i=1}^{10} \frac{\gamma_i^2}{\Omega_i^2 + \omega^2} \tag{S3}$$

We assume that there is no temperature dependence of $\varepsilon(i\omega)$ for all solid substrates considered, and that $\varepsilon_{vap} \approx 1$ for saturated vapor for all relevant temperatures (upto 550K). Calculated dispersions for all solid materials are shown in Figure S1a. Calculated $\varepsilon_{2\perp,\parallel}$ for all solid materials considered are shown in Figure S2.

S1.1 Temperature dependence of water complex permittivity

We utilize experimental data measured at saturation over the relevant temperature range for the static permittivity of water [3] , shown in Figure S1b. For its complex permittivity we utilize the experimental dispersion data from Ref. [1] shown in Figure S1c with solid symbols. The complex permittivity must be treated more carefully, as it reduces towards that of the saturated vapor with increasing temperature (they are indistinguishable at T_c). As a simple heuristic, we use the Havriliak–Negami relaxation model for the temperature dependent complex permittivity of water[4],

$$\varepsilon(i\omega, T)_{HN} = 1 + \frac{\varepsilon 0(T) - 1}{(1 + (\omega\tau)^n)^m} \tag{S4}$$

where we use $\tau = 2$ps as the dipole relaxation timescale, $n = 2$ and $m = 1$. We utilize experimental data shown in Figure S1b for the static permittivity of water $\varepsilon 0(T)$. Normalizing Eq. (S4) with its value at 300K, we obtain a function that describes the attenuation of the dispersion at any frequency:

$$f(T) = \frac{\varepsilon(i\omega, T)_{HN}}{\varepsilon(i\omega, 300)_{HN}} \tag{S5}$$

Multiplying this scaling function with the experimental fit for water, Eq. (S3), we obtain a heuristic temperature dependence of the dispersion of water as shown in

Supplementary Figure 1

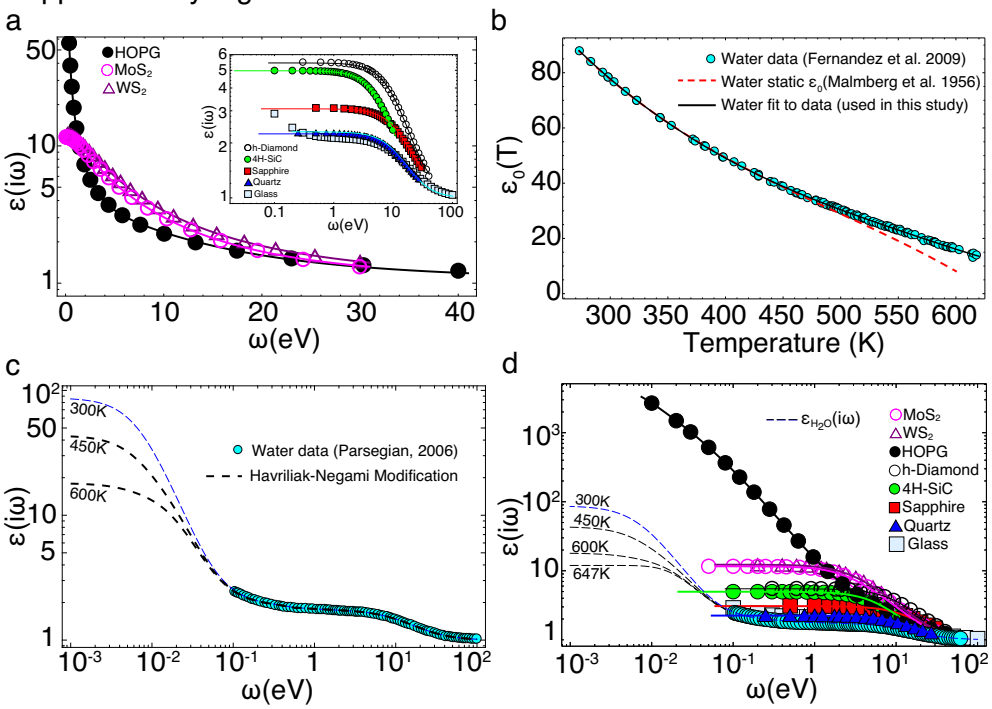

Fig. S1 Dielectric dispersion for all materials materials used in this study. a. Temperature-independent dispersion for solid materials. The solid lines show fits to the dispersion extracted by Kramers-Kronig analysis. The outer figure for 2D materials shows fits using a 12-term sum-over-oscillator series, while the inset shows single-oscillator fits for insulators. b. Temperature dependent behavior of the static dielectric permittivity of water along the saturation line. The data and fit used for this study are depicted by cyan markers and the solid black line, while an earlier experimental benchmark is depicted by the dashed red line. c. Dielectric dispersion of water over a wide range of frequencies. Cyan markers show data given in Ref. [1], and the blue line represents the fit to the data. The blue line is a piece-wise function, with one part comprising of the fit to the full range of experimental data (cyan markers; $0.1 - 100$ eV) using a 12-term sum-over-oscillator series, while the "static" part comprises of a fit to the data in the range $\omega < 0.7$eV in addition to the static part $\varepsilon(0) = 88$. The dashed black lines depict the heuristic of mapping the Havriliak-Negami relaxation model with the data in b. to the full dispersion. Temperature ceases to have an effect on the dispersion above ~ 0.1eV. d. All dispersion data plotted together to depict the strengths of the dielectric dispersions, and suggest the strength of the Hamakers constant - which is small when the dispersions are close together.

Figure S1c, with dashed lines showing the temperature dependence of the modified dispersion. We find that any temperature dependence is confined to infra-red regimes below 0.1 eV, which is lower than the first Matsubara frequency at room temperature (0.15eV). For higher relaxation times, such as those suggested by recent simulations[5],

the frequency cut-off for temperature dependence is even lower. Figure S1d overlays the dispersion of all materials on a log-log scale, providing a visual queue describing the van der Waals attraction between any two materials, where greater differences in permittivity result in higher vdW attraction.

S2 Calculating Hamaker's constants

Hamakers constants between two pairs of materials in a background of a third material are calculated by sampling the corresponding permittivities over Matsubara frequencies, which are derived from treating each medium m as a collection of oscillators each with energy $g_j = -k_B T \ln Z(\omega_j)$ where $Z(\omega_j) = \sum_{n=0}^{\infty} \exp(-E_{n,j}/k_B T)$ is the partition function and $E_{n,j} = \hbar\omega_j \left(n + \frac{1}{2}\right)$ are the energy levels with eigenmodes n of the simple harmonic oscillator, and requiring that these should be summed over each "surface mode" j of electromagnetic waves with radial wavevectors $\rho_m = \rho - \frac{\varepsilon_m \mu_m \omega^2}{c^2}$ that are characterized by the boundary conditions of Maxwell's equations at the interfaces and at infinity, for all possible values of ρ[1]. The full formulation accounts for electromagnetic retardation at large distances when the effect of high frequencies do not have sufficient time to propagate the requisite distance to contribute to modifying the fluctuations, and includes the contrast in magnetic permeabilities μ for all materials interfaces. For our purpose, we ignore the contributions of μ of the materials to the full Hamaker's constant, which typically have a negligible effect beyond optical frequencies, where they take on the value of that of free space ($\mu_{ij} = 1$), and consider only the nonretarded formulation of Hamaker's constant for small length scales $\lesssim 10^3$Å such as those pertinent for the effects of adsorption.

S2.1 Plane-Plane interactions

Based on the theory of Dzyaloshinskii, Lifshitz, and Pitaevskii[6], the interaction between materials 1 and 2 separated by a medium 3, A_{132}, is computed from dielectric

contrasts at imaginary Matsubara frequencies $\omega_n = (2\pi)^2 n k_B T/\hbar$ as,

$$A_{132} = \frac{3k_B T}{2} \sum_{n=0}^{\infty}{}' \left[\Delta_{13}(i\omega_n) \cdot \Delta_{23}(i\omega_n)\right] \tag{S6}$$

$$\Delta_{ij}(i\omega_n) = \frac{\varepsilon_i(i\omega_n) - \varepsilon_j(i\omega_n)}{\varepsilon_i(i\omega_n) + \varepsilon_j(i\omega_n)} \tag{S7}$$

where k_b is Boltzman's constant, T is the temperature, the prime denotes a half-weight on $n = 0$, and ε_i, $\varepsilon_i(i\omega)$ are the static and complex dielectric permittivities of materials i respectively, which has been calculated in the previous section. This expression assumes negligible magnetic contributions ($\mu_{ij} = 1$) and uses the non-retarded approximation, appropriate for nanometric film thicknesses[1]. The Hamaker constant thus separates into static and dispersive contributions

$$A_{132} = A_{stat} + A_{disp} \tag{S8a}$$

$$A_{stat} \approx \frac{3}{4} k_b T \Delta_{13} \Delta_{23} \tag{S8b}$$

$$A_{disp} \approx \frac{3\hbar}{4\pi} \int_{\omega_1}^{\infty} \Delta_{13}(i\omega_n)\Delta_{23}(i\omega_n) d\omega \tag{S8c}$$

where we have used the transform $k_B T \sum_{n=1}^{\infty} \longrightarrow \frac{\hbar}{2\pi} \int_{\omega_1}^{\infty} d\omega$[2].

For all temperatures we set the lower limit of the integral in Eq. (S8c) to 0.1eV, which is lower than, for example, the first Matsubara frequency at 550K (0.3eV). Thus we realistically exclude any temperature dependence of the dispersive term. We choose the fixed lower limit for the dispersion integrals because it consistently exhibits only a small deviation of the calculated Hamaker's constant from that calculated using the explicit sum over a wide range of temperatures. The deviation is smaller at higher temperatures. In the most extreme case (HOPG-vacuum-HOPG), we find a deviation under 6% at 300K which reduced to 5% at 500K. Additionally, the integral is much faster to compute than the sum, and allows for easily broadcasting

the computation to multiple materials interfaces over continuous temperatures. The results of the calculation of A_{SLV} for different configurations are shown in Figure S3.

S2.2 Atom-surface interactions

The simple adsorption model uses a general potential for the interaction between an adsorbate molecule and a half-plane of substrate separated by vacuum that has been shown to be a van der Waals' interaction $\sim -C_3/z^3$, where C_3 is the Lifshitz–van-der Waals Hamaker constant for atom-surface interactions. For such interactions, C_3 is derived from the total polarizability α_{tot} of the adsorbate which is comprised of a dispersive part due to dipole- induced-dipole and induced-dipole-induced-dipole fluctuations, α_{ind}, and a static part α_{perm} due to the permanent dipole moment μ_{dip} of water and the static dielectric contrast of the substrate with the vacuum (also known as the surface response function)[1, 7, 8]. For adatoms with a permanent dipole moment, the corresponding equations are

$$C_3 = \frac{k_B T}{2} \sum_{n=0}^{\infty} \frac{\alpha_{tot}(i\omega_n)}{4\pi\varepsilon_m(i\omega_n)} \Delta_{Am}(i\omega_n) \tag{S9a}$$

$$\alpha_{tot}(i\omega_n) = \alpha_{ind} + \alpha_{perm} \tag{S9b}$$

$$\alpha_{ind}(i\omega) = a^3 \left[\frac{\varepsilon_a(i\omega) - \varepsilon_m(i\omega)}{\varepsilon_a(i\omega) + 2\varepsilon_m(i\omega)} \right] \tag{S9c}$$

$$\alpha_{perm} = \frac{\mu_{dip}^2}{3kT(1+\omega\tau)} \tag{S9d}$$

where $\varepsilon_m = 1$ (in gaussian units) for taking the background to be the vacuum, a is the spherical radius of the water molecule, and τ is a dipole relaxation time scale of water, which is large enough that the term does not present in the dispersive part of Eq. (S9a); thus we take $\omega \to 0$ in Eq. (S9d). Converting from gaussian to mks units, and then to cgs units using $\alpha_{gauss} * \varepsilon_0 = \alpha_{\text{mks}}$ and $\alpha_{\text{mks}} = 4\pi\varepsilon_0\alpha_{\text{cgs}}$, Eq. (S9c) becomes

$\alpha_{ind}(i\omega)_{\text{mks}} = \alpha_0 \widetilde{\Delta}_{LV}$ where $\alpha_0 = 4\pi\varepsilon_0 a^3$ is the static polarizability volume of the adsorbate in cgs units, and $\widetilde{\Delta}_{LV}(i\omega)$ represents the term in brackets in Eq. (S9c) and inherits the same convention as Eq. (S7). Once again, we make the low-temperature sum-to-integral transformation for Eq. (S9a), to obtain $C_3 = C_{3_{\text{disp}}} + C_{3_{\text{stat}}} + C_{3_{\text{perm}}}$ paralleling Eqs. (S8a) - (S8c) where

$$C_{3_{\text{disp}}} = \frac{\hbar}{4\pi} \int_{\omega_1}^{\infty} \alpha_0 \widetilde{\Delta}_{LV}(i\omega) \Delta_{SV}(i\omega) d\omega \tag{S10a}$$

$$C_{3_{\text{stat}}} = \frac{1}{4} k_B T \alpha_0 \widetilde{\Delta}_{LV} \Delta_{SV} \tag{S10b}$$

$$C_{3_{\text{perm}}} = \frac{\mu_{\text{dip}}^2}{12} \Delta_{SV} \tag{S10c}$$

This expression for the Lifshitz-C_3, which is valid for dilute gases, is equivalent to that used in previous studies on the simple model[7, 9–13] except that we do not make the single-excitation Drude-model approximation for the polarizability of water. To better model the temperature dependent wetting of highly polar molecules, we utilize the theoretically predicted temperature dependence of μ_{dip} and α_0 from the modified Onsager-Kirkwood-Fröhlich theory[14]. We note that in the temperature regime relevant to this experiment, $\alpha_0 \sim 5.3\text{Å}^3$ while μ_{dip} exhibits a roughly linear 15% decrease, starting at 2.8D at 300K. Additionally, we find that the contribution of the permanent dipole moment of water is approximately one-third ($\sim 32 \pm 4\%$) of the total C_3, and is primarily responsible for the temperature dependence of C_3, being over ten times larger in magnitude than the static part of C_3.

S2.3 Comparison of Hamaker Constants

C_3 is an analogue of A_{SVL}, the interaction between a substrate and adsorbate acting across a vacuum, and thus they can be compared by $6\pi\Delta\rho C_3 = A_{SVL}$. Calculations of all components of C_3 and finally its comparison to both A_{SVL} and A_{SLV} is shown in Table S1:

Substrate	$C_{3_{\text{disp}}}$	$C_{3_{\text{stat}}}$	$C_{3_{\text{perm}}}$	C_3	$6\pi A_{SLV}/\rho C_3$	$6\pi A_{SVL}/\rho C_3$
4H-SiC [15]	601.3	27.1	331.1	959.5	0.4399	0.8096
HOPG [16, 17]	674.9	29.0	354.6	1058.5	0.5156	0.8234
Quartz [18]	420.2	19.3	236.1	675.7	0.2212	0.8077
Sapphire [19]	621.6	27.1	330.8	979.5	0.4444	0.8253
(H) Diamond [20]	825.0	23.2	284.0	1132.2	0.6537	0.9368
WS_2 [21]	824.9	26.9	328.4	1180.1	0.6469	0.8979
MoS [22]	767.4	27.3	334.2	1129.0	0.6014	0.8737
Glass [23]	426.8	19.3	236.1	682.2	0.2325	0.8121

Supplementary Materials Table S1 Data from experimental optical data of C_3 in meV Å^3 with the dispersion of water taken at 300K. The substrate-vapor adhesion through liquid C_3 is significantly smaller for Quartz and Glass than that for the other materials, suggesting that short-ranged effects may play a bigger role as $T \to T_w$. The last two columns compare the A's against C_3, and show that A_{SVL} is better matched with C_3 as both consider the adhesion of water with a substrate in a vacuum background.

As expected the Hamaker's constant A_{SLV} calculated in the previous section is quite different from the calculated C_3, while A_{SVL} is within 20% of C_3. Because we utilize free parameters in this study (h_{eq} for the thermodynamic model and the well depth for the simple model), the precise value of the interaction strength does not matter as much as its temperature dependence to explain the temperature dependence of the contact angle.

S3 Thin-film Perturbation to V_{39} Potential

Let $V_{tot_r}(z_r, d_r)$ represent the total potential $V_{tot}(z)$ in terms of reduced variables. Apply a perturbation to its point of closest approach, which should be linear in deviated parameters dC and dD for small deviations: $\tilde{z} \equiv z_{r_{min}} + A \cdot dC + B \cdot dD$. Being an extremum, $\tilde{z}$ is set as the solution to the equation $\Delta V(z_r, d_r) \equiv \frac{dV_{tot_r}(z_r, d_r)}{dz_r}|_{\tilde{z}} = 0$. Expanding $\Delta V(z_r, d_r)$ in a Taylor series to first order around $dC, dD = 0$

$$\begin{aligned}\Delta V(z_r, d_r) &\approx \sum_{n,m=0}^{n,m=\infty} \frac{dC^n dD^m}{n!m!} \cdot \frac{\partial^{n+m} \Delta V'(z')}{\partial dC^n \partial dD^m} \\ &\approx \frac{1}{27} dC \cdot D_1(a_1 + a_2 \cdot A) \\ &+ \frac{1}{27} dD \cdot D_1(b_1 + b_2 \cdot B)\end{aligned} \tag{S11}$$

we find the criteria for A and B in terms of the constants a_1, a_2, b_1, b_2 (which are determined by d_r) - the trailing terms in parentheses in Eq. (S11) should simultaneously vanish to describe the minimum of the perturbed potential. Given a reduced integral and point of closest approach, we can evaluate the integral again using a Taylor Series expansion to first order in dC and dD:

$$\begin{aligned} I &\equiv (\frac{C_{31}}{D_1})^{1/3} \int_{\tilde{z}}^{\infty} V_{tot_r}(z_r, d_r) dz_r \\ &= (C_{31} D_1^2)^{1/3} (-0.601 + X dC + Y dD) \end{aligned} \tag{S12}$$

where X and Y depend on d_r, as shown in Figure S4.

S4 Dielectric dispersion for monolayer coated materials

Having calculated C_3 from perturbation theory, we can decompose it into its static and dynamic parts, and calculate the dispersion of the modified substrate using Eq. (S2). A third parameter is then the$\varepsilon 0$ appearing in Eq. (S10b), which should also be extracted from the fit. This data is presented in the main text.

S5 Experimental Methods

We selected our substrates based on their relative polarities, chemical and/or structural similarity to graphene, and applicability in wide ranging industries.

The polarity of the single crystal CVD diamond is the most tunable on the surface as it depends on how the surface carbon 'dangling bonds' are terminated. The original sample with $< 100 >$ crystallographic orientation (*Element Six*, Santa Clara, CA) was oxygen terminated by acid cleaning after production. We then followed a reversible

technique to convert the o-diamond to h-diamond by annealing it at 850 ° C at atmospheric pressure in the presence of hydrogen gas[24]. Because fluorine terminated diamond has been proposed as a solution for hydrophobic devices with enhanced resistance to oxygenation[25, 26], we fluorinated the sample in a plasma etcher at room temperature and chamber pressure of 50 mTorr by flowing C_4F_8 at 100 sccm for 100 seconds, with RF power of 200 W[25]. The hydrogen- and fluorine- terminated samples were imaged as soon as they became ready, without further cleaning steps.

We selected 4H-SiC (4H-polytype with crystallographic orientation (0001)) and monolayer-graphene epitaxially grown on 4H-SiC(henceforth termed "1L-graphene", from *Graphensic AB*, Linköping, Sweden) for their relatively simple crystal structures. They also address the controversy surrounding the wetting transparency of graphene[27–32] by providing the bulk and composite materials using which we could test our perturbation theory. Before each trial, these samples were cleaned with acetone followed by isopropyl alcohol to remove any adsorbed airborne hydrocarbons and other debris, followed by DI water to wash off the organic solvents and passivate the surface. Then they were dried in a closed environment.

We used the same experimental apparatus and imaging techniques as in Ref. [12] to generate our data. The wetting transition over 4H-SiC and 1L-graphene was recorded in two ways. The first was by directly imaging the sessile drop resting on the substrate. The high contrast profile of the drop was fitted to the Young-Laplace equation $\Delta P_0(r) + \Delta\rho g z(r) = \sigma_{LV}\kappa$, where κ is the total curvature, $z(r)$ is the height of the drop, and $\Delta P_0(r) = P_L - P_V$ is the difference in pressure between liquid and vapor phases at the surface at distance r from the center of the drop, and $\Delta\rho = \rho_L - \rho_V$ is the mass density difference between liquid and vapor phases. Using $\kappa(z) = \frac{1+(r'(z))^2 - r(z)r''(z)}{r(z)(1+(r'(z))^2)^{3/2}}$ in cylindrical coordinates for an axisymmetric drop in the

Young-Laplace equation, the resulting second order differential equation satisfying the conditions $r'(z = H) = r(H) = 0$ (where H is the maximum height of the drop at the center) was solved numerically to return the total drop profile $r(z)$ that best matches the experimental data. Because of the global fit that could be tuned to match the high contrast portions of the drop shape in any image, we have high confidence in the macroscopic θ extracted in this way. Because the cell was sealed at room temperature, the pressure inside the cell was determined from the saturated vapor pressure of water at any temperature. Establishing a saturated vapor pressure is critical for the sessile drop to remain in the liquid phase even at high temperatures, and allows us to drop any gradients in the chemical potential. A good approximation to estimate the saturated vapor pressure is given by the Antoine equation[33], with saturated vapor pressure inside the wetting cell reaching 55.8 atm at 544K[34]. Despite precautions to maintain an isothermal environment within the wetting cell, we estimate a $\sim 1°$C temperature difference between the center of the cell where the substrate was placed and its boundaries, which were radiatively heated, resulting in condensation on the surface of the cell. The second recording of the wetting transition was to image the vertical face of the crystal surface and mark the temperature when the wetting behavior transitions from drop-wise to film-wise condensation at T_w. Details of the fit and associated errors are discussed in Ref. [12].

For all materials, $\varepsilon(i\omega)$ was calculated from the Kramers-Kronig analysis of experimental optical constants performed on Mathematica. Data was extracted manually from published material containing tabulated values (Quartz, Diamond, Glass). Data was extracted from plots using the freely available WebPlotDigitizer tool [35]. The data was verified by super imposing onto the original image. For HOPG and MoS_2, we use previously reported fits to $\varepsilon(i\omega)$[36]. We use data extracted from Refs. [16, 17] for greyed points in Figure 5 b of the main text.

The various materials properties and constants required for this study are cited below.

Parameter	Reference	value type	value
$\Delta\rho_{LV}$	[37]	data set	fit function
σ_{LV}	[38]	fit equation	fit function
radius (oxygen, fluorine, carbon)	[39]	constants	3.24, 3.082, 3.609 bohr
Monolayer Thickness Graphene	[40]	constant	3.45 Å
Monolayer Thickness WS_2	[41]	constant	6.16 Å
Monolayer Thickness MoS_2	[42]	constant	6.5 Å
$\varepsilon 0$ 4H-SiC	[43]	constant	9.99
$\varepsilon 0$ Diamond	[44]	constant	5.7
$\varepsilon 0$ HOPG		constant	15.12
$\varepsilon 0$ quartz (α-SiO_2)		constant	3.8
$\varepsilon 0$ sapphire (α-Al_2O_3)	[19]	constant	9.9
$\varepsilon 0$ glass (a-SiO_2)		constant	3.8
$\varepsilon 0$ WS_2	[45]	constant	9.6
$\varepsilon 0$ MoS_2	[45]	constant	10.5
ε_2 4H-SiC	[15]	data set	KK analysis
ε_2 HOPG	[36]	data set	KK analysis
ε_2 Quartz	[18]	data set	KK analysis
ε_2 Sapphire	[19]	data set	KK analysis
ε_2 (H) Diamond	[20]	data set	KK analysis
ε_2 WS_2	[21]	data set	KK analysis
ε_2 MoS	[22]	data set	KK analysis
ε_2 Glass	[23]	data set	KK analysis

Supplementary Materials Table S2 Other experimental data and constants

References

[1] Parsegian, V. A. *Van der Waals Forces: A Handbook for Biologists, Chemists, Engineers, and Physicists* (Cambridge University Press, 2005).

[2] Israelachvili, J. N. *Intermolecular and Surface Forces* 3 edn (2011). URL https://doi.org/10.1016/b978-0-12-375182-9.10011-9.

[3] Fernández, D. P., Mulev, Y., Goodwin, A. R. H. & Sengers, J. M. H. L. A database for the static dielectric constant of water and steam. *Journal of Physical and Chemical Reference Data* **24**, 33–70 (1995). URL https://doi.org/10.1063/1.555977.

[4] Raicu, V. & Feldman, Y. *Dielectric Relaxation in Biological Systems: Physical Principles, Methods, and Applications* (Oxford University Press, 2015). URL https://doi.org/10.1093/acprof:oso/9780199686513.001.0001.

[5] Zarzycki, P. & Gilbert, B. Temperature-dependence of the dielectric relaxation of water using non-polarizable water models. *Phys. Chem. Chem. Phys.* **22**, 1011–1018 (2020). URL https://doi.org/10.1039/c9cp04578c.

[6] Dzyaloshinskii, I., Lifshitz, E. & Pitaevskii, L. The general theory of van der waals forces. *Advances in Physics* **10**, 165–209 (1961). URL https://doi.org/10.1080/00018736100101281.

[7] Vidali, G. & Cole, M. The interaction between an atom and a surface at large separation. *Surface Science* **110**, 10–18 (1981). URL https://doi.org/10.1016/0039-6028(81)90584-7.

[8] Bruch, L. W., Cole, M. W. & Zaremba, E. *Physical Adsorption: Forces and Phenomena* (Oxford University Press, 1997). URL https://doi.org/10.1093/oso/9780198556381.001.0001.

[9] Cheng, E., Cole, M. W., Saam, W. F. & Treiner, J. Helium prewetting and nonwetting on weak-binding substrates. *Physical Review Letters* **67**, 1007–1010 (1991). URL https://doi.org/10.1103/PhysRevLett.67.1007.

[10] Vidali, G., Ihm, G., Kim, H.-Y. & Cole, M. W. Potentials of physical adsorption. *Surface Science Reports* **12**, 135–181 (1991). URL https://doi.org/10.1016/

0167-5729(91)90012-m.

[11] Gatica, S. M., Johnson, J. K., Zhao, X. C. & Cole, M. W. Wetting transition of water on graphite and other surfaces. *Journal of Physical Chemistry B* **108**, 11704–11708 (2004). URL https://doi.org/10.1021/jp048509u.

[12] Friedman, S. R., Khalil, M. & Taborek, P. Wetting transition in water. *Physical Review Letters* **111**, 1–5 (2013). URL https://doi.org/10.1103/PhysRevLett.111.226101.

[13] Kim, H.-Y., Santos, D., Cristina, M. & Cole, M. W. Wetting transitions of water on graphite and graphene. *The Journal of Physical Chemistry A* **118**, 8237–8241 (2014). URL https://doi.org/10.1021/jp501046r.

[14] Putintsev, D. N. & Putintsev, N. M. *The theoretical study of dielectric properties of water using the modified onsager-kirkwood-fröhlich theory*, 1–5 (2019). URL https://doi.org/10.1109/icdl.2019.8796591.

[15] Lindquist, O., Schubert, M., Arwin, H. & Järrendahl, K. Infrared to vacuum ultraviolet optical properties of 3c, 4h and 6h silicon carbide measured by spectroscopic ellipsometry. *Thin Solid Films* **455-456**, 235–238 (2004). URL https://doi.org/10.1016/j.tsf.2004.01.008.

[16] Taft, E. A. & Philipp, H. R. Optical properties of graphite. *Physical Review* **138**, A197–a202 (1965). URL https://doi.org/10.1103/PhysRev.138.A197.

[17] Tosatti, E. & Bassani, F. Optical constants of graphite. *Il Nuovo Cimento B Series 10* **65**, 161–173 (1970). URL https://doi.org/10.1007/bf02711192.

[18] Philipp, H. in - *silicon dioxide (sio2), type α (crystalline)* (ed.Palik, E. D.) *Handbook of Optical Constants of Solids* 719–747 (Academic Press, Burlington,

1997). URL https://doi.org/10.1016/b978-012544415-6.50037-6.

[19] Harman, A. K., Ninomiya, S. & Adachi, S. Optical constants of sapphire (α-al2o3) single crystals. *Journal of Applied Physics* **76**, 8032–8036 (1994). URL https://doi.org/10.1063/1.357922.

[20] Edwards, D. F. & Philipp, H. R. *Cubic Carbon (Diamond)*, 665–673 (Academic Press, Boston, 1985). URL https://doi.org/10.1016/b978-0-08-054721-3.50035-6.

[21] Beal, A. R., Liang, W. Y. & Hughes, H. P. Kramers-kronig analysis of the reflectivity spectra of 3r-ws2 and 2h-wse2. *Journal of Physics C: Solid State Physics* **9**, 2449–2457 (1976). URL https://doi.org/10.1088/0022-3719/9/12/027.

[22] Beal, A. R. & Hughes, H. P. Kramers-kronig analysis of the reflectivity spectra of 2h-mos_2, 2h-mose_2and 2h-mote_2. *Journal of Physics C: Solid State Physics* **12**, 881–890 (1979). URL https://doi.org/10.1088/0022-3719/12/5/017.

[23] Philipp, H. in - *silicon dioxide (sio2) (glass)* (ed.Palik, E. D.) *Handbook of Optical Constants of Solids* 749–763 (Academic Press, Burlington, 1997). URL https://doi.org/10.1016/b978-012544415-6.50038-8.

[24] Seshan, V. *et al.* Hydrogen termination of cvd diamond films by high-temperature annealing at atmospheric pressure. *Journal of Chemical Physics* **138** (2013). URL https://doi.org/10.1063/1.4810866.

[25] Schvartzman, M. & Wind, S. J. Plasma fluorination of diamond-like carbon surfaces: mechanism and application to nanoimprint lithography. *Nanotechnology* **20**, 145306 (2009). URL https://doi.org/10.1088/0957-4484/20/14/145306.

[26] Patterson, D. E., Hauge, R. H. & Margrave, J. L. Fluorinated diamond films, slabs, and grit. *MRS Proceedings* **140**, 351 (2011). URL https://doi.org/10.1557/

proc-140-351.

[27] Rafiee, J. *et al.* Wetting transparency of graphene. *Nature Materials* **11**, 217–222 (2012). URL https://doi.org/10.1038/nmat3228.

[28] Shih, C. J. *et al.* Breakdown in the wetting transparency of graphene. *Physical Review Letters* **109** (2012). URL https://doi.org/10.1103/PhysRevLett.109.176101.

[29] Shih, C. J., Strano, M. S. & Blankschtein, D. Wetting translucency of graphene. *Nature materials* **12**, 866–869 (2013). URL https://doi.org/10.1038/nmat3760.

[30] Driskill, J., Vanzo, D., Bratko, D. & Luzar, A. Wetting transparency of graphene in water. *The Journal of Chemical Physics* **141** (2014). URL https://doi.org/10.1063/1.4895541.

[31] Kim, D., Pugno, N. M., Buehler, M. J. & Ryu, S. Solving the controversy on the wetting transparency of graphene. *Scientific Reports* **5** (2015). URL https://doi.org/10.1038/srep15526.

[32] Bera, B. *et al.* Wetting of water on graphene nanopowders of different thicknesses. *Applied Physics Letters* **112**, 151606 (2018). URL https://doi.org/10.1063/1.5022570.

[33] Thomson, G. W. The antoine equation for vapor-pressure data. *Chemical Reviews* **38**, 1–39 (1946). URL https://doi.org/10.1021/cr60119a001.

[34] DortmundDataBank. Saturated vapor pressure. URL http://ddbonline.ddbst.com/AntoineCalculation/AntoineCalculationCGI.exe?component=Water.

[35] Rohatgi, A. Webplotdigitizer: Version 4.5. *URL https://automeris. io/WebPlotDigitizer* **411** (2020).

[36] Krajina, B. A., Kocherlakota, L. S. & Overney, R. M. Direct determination of the local hamaker constant of inorganic surfaces based on scanning force microscopy. *The Journal of Chemical Physics* **141**, 164707 (2014). URL https://doi.org/10.1063/1.4898799.

[37] Wagner, W. & Pruß, A. The iapws formulation 1995 for the thermodynamic properties of ordinary water substance for general and scientific use. *Journal of Physical and Chemical Reference Data* **31**, 387–535 (2002). URL https://doi.org/10.1063/1.1461829.

[38] Vargaftik, N. B., Volkov, B. N. & Voljak, L. D. International tables of the surface tension of water. *Journal of Physical and Chemical Reference Data* **12**, 817 (1983). URL https://doi.org/10.1063/1.555688.

[39] Charry, J. & Tkatchenko, A. van der waals radii of free and bonded atoms from hydrogen (z = 1) to oganesson (z = 118). *Journal of Chemical Theory and Computation* **20**, 7469–7478 (2024). URL https://doi.org/10.1021/acs.jctc.4c00784.

[40] Soldano, C., Mahmood, A. & Dujardin, E. Production, properties and potential of graphene. *Carbon* **48**, 2127–2150 (2010). URL https://doi.org/https://doi.org/10.1016/j.carbon.2010.01.058.

[41] Chaves, A. *et al.* Bandgap engineering of two-dimensional semiconductor materials. *npj 2D Materials and Applications* **4**, 29 (2020). URL https://doi.org/10.1038/s41699-020-00162-4.

[42] Novoselov, K. S. *et al.* Two-dimensional atomic crystals. *Proceedings of the National Academy of Sciences* **102**, 10451–10453 (2005). URL https://doi.org/10.1073/pnas.0502848102.

[43] SurfaceNet. Silicon carbide (sic). URL https://surfacenet.de/files/old_version/html/sic.html.

[44] Sussmann, R. S. *CVD Diamond for Electronic Devices and Sensors* (John Wiley & Sons, 2009).

[45] Laturia, A., Van de Put, M. L. & Vandenberghe, W. G. Author correction: Dielectric properties of hexagonal boron nitride and transition metal dichalcogenides: from monolayer to bulk. *npj 2D Materials and Applications* **4**, 28 (2020). URL https://doi.org/10.1038/s41699-020-00163-3.

Supplementary Figure 2

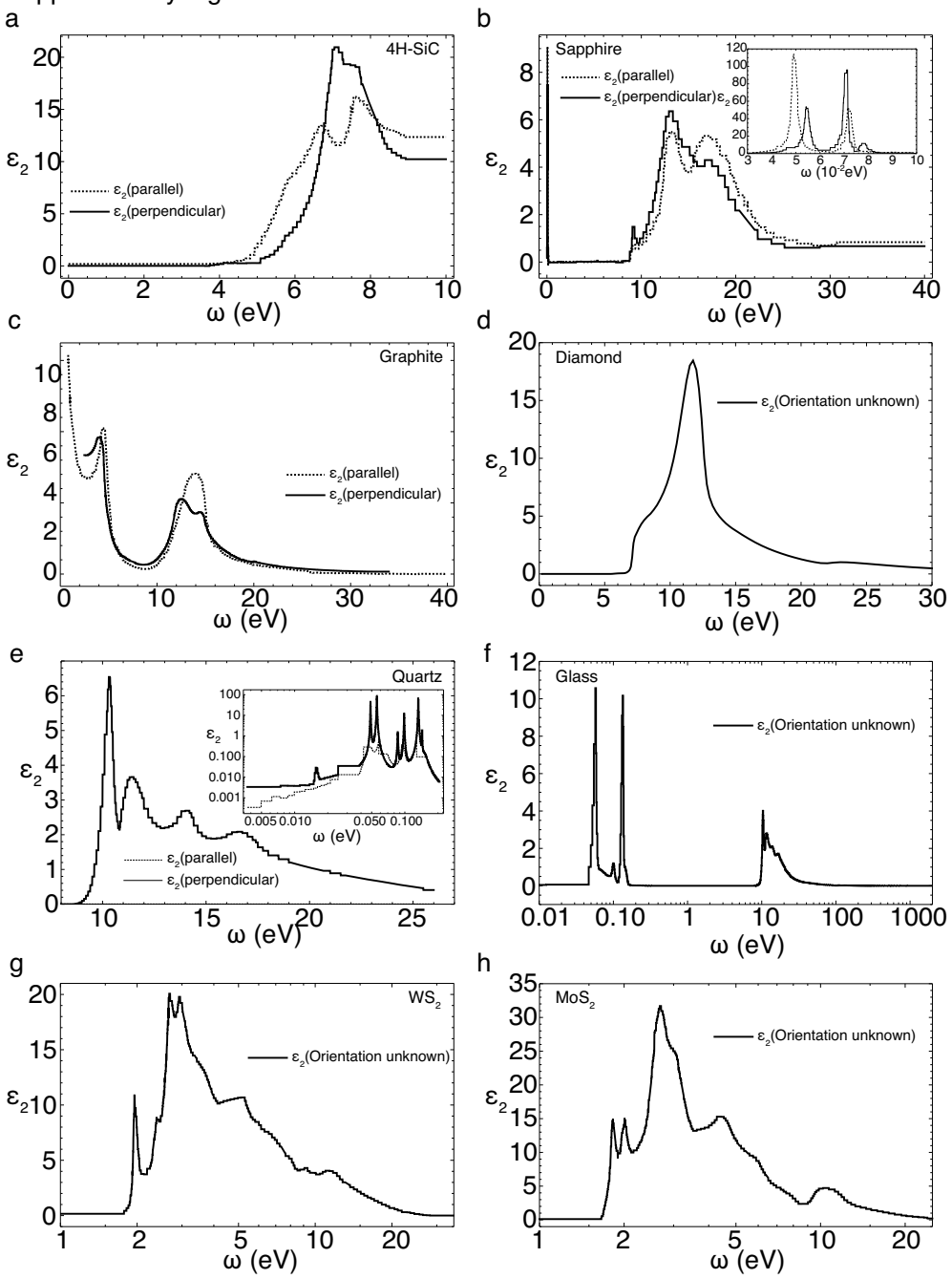

Fig. S2 Dielectric surface response function calculated from data presented in Figure S1 over the available range of frequency (dashed blue line) and fitted by a Lorentzian model with two fitting parameters g_0 and ω_s (solid black line) for a) 4H-SiC, b) Sapphire, c) Graphite, d) Diamond, e) Quartz, f) Glass, g) WS_2, and h) MoS_2.

Supplementary Figure 3

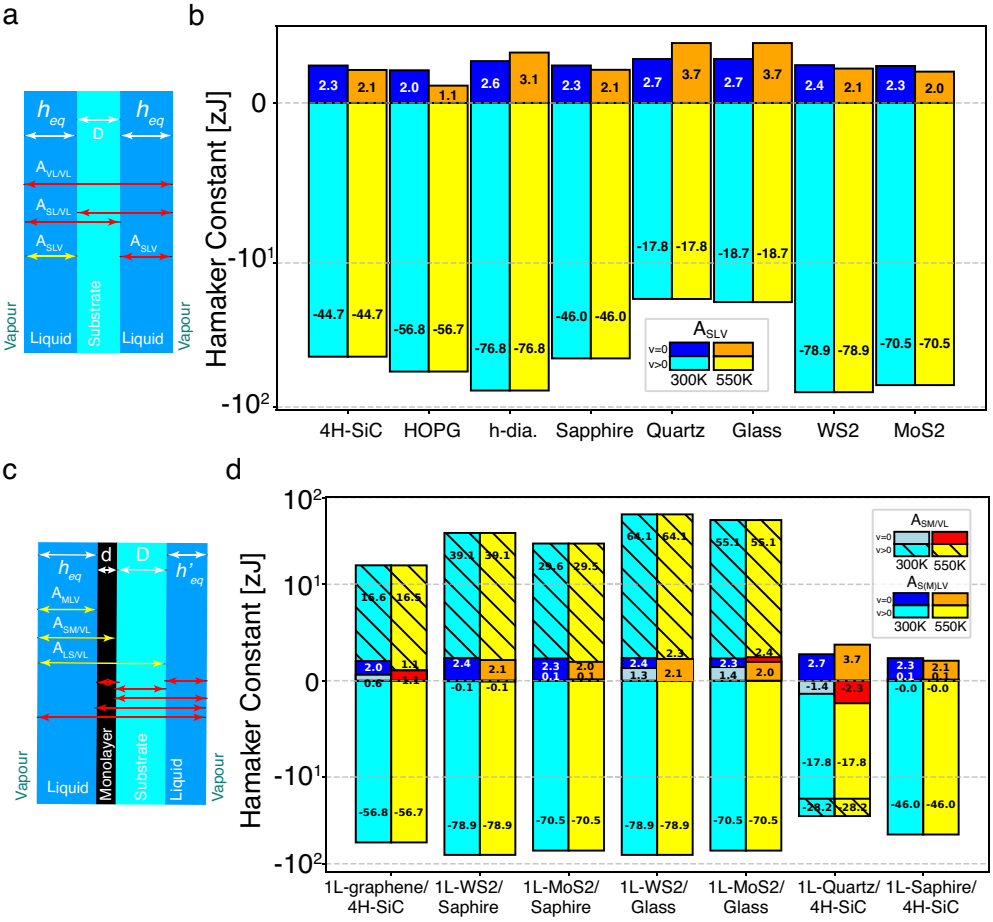

Fig. S3 Evaluation of the Hamakers constant using the schematic of (a.) wetting over a bulk substrate with thickness D, and a wetting film with thickness h_{eq} , and (b.) wetting over a bulk substrate covered by a monolayer of thickness d. Because $D >> x > x$, we ignore the contributions of wetting from the other side of the underlying substrate (labeled by adsorption layer thickness h_{eq} and h'_{eq} respectively. c. Calculated components of Hamaker's constant for various materials used in this study, where blue and orange boxes represent $A_{\omega=0}$ for bulk substrates at two different temperatures, and grey-blue and red boxes represent the same for the monolayer composite. Cyan and yellow boxes represent $A_{\omega>0}$ for all materials at T = 300K and 500K respectively. The hatched area depicts the interaction between the substrate-monolayer interface and the liquid-vapor interface. In all cases the static contribution is an order of magnitude less than that due to dispersion, while the contribution to the total Hamakers constant due to the monolayer is over 3 times that from the substrate when it is screened by the monolayer.

Supplementary Figure 4

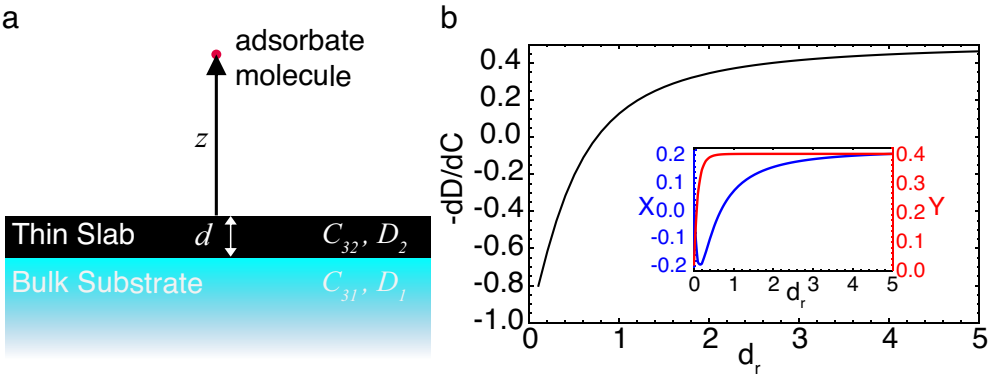

Fig. S4 a. Schematic of binding interaction of a composite comprising of a thin film slab capping a bulk substrate on an adsorbate molecule. b. Condition for transparency as 'reduced' thickness increases. For $d_r < 0.75$, dC must have same sign as dD for transparency. For monolayer films and beyond, dC and dD must have opposite signs (compensating one another) to establish transparency. The crossover occurs when $d_r \sim 0.75$, and the ratio $-dD/dC$ asymptotically approaches ~ 0.5 as $d_r \to \infty$.